Research Square

Preprints are preliminary reports that have not undergone peer review.
They should not be considered conclusive, used to inform clinical practice,
or referenced by the media as validated information.

Pressure-Induced Structural Phase Transitions in MBANP: A First-Principles Study of Elastic, Phonon, and Optical Properties

Yi-Gao Wang

w_yigao@126.com

Jiujiang University

Dong-Yang Wang

Jiujiang University

Liang-Liang Zhou

Jiujiang University

Zhen Jiao

Southwest Jiaotong University

Mi Zhong

Southwest Jiaotong University

Research Article

Keywords: First-principles, MBANP, High pressure, Elastic properties, Optical Properties

Posted Date: August 12th, 2026

DOI: https://doi.org/10.21203/rs.3.rs-10521717/v1

License: This work is licensed under a Creative Commons Attribution 4.0 International License.
Read Full License

Additional Declarations: No competing interests reported.

Pressure-Induced Structural Phase Transitions in MBANP: A First-Principles Study of Elastic, Phonon, and Optical Properties

Yi-Gao Wang[a,b,*], Dong-Yang Wang[a], Liang-Liang Zhou[a], Zhen-Jiao[c], Mi-Zhong[d]

[a]Department of Physics, Jiujiang University, Jiujiang 332005, China

[b]Jiangxi Province Key Laboratory of Surface Engineering, Jiujiang 332005, China

[c]Bond and Band Engineering Group, School of Physical Science and Technology, Southwest Jiaotong University, Chengdu 610031, People's Republic of China

[d]School of Sciences, Southwest Petroleum University, Chengdu 610500, People's Republic of China

[*] Corresponding author at: Department of Physics, Jiujiang University, Jiujiang 332005, China

E-mail address: w_yigao@126.com.

Abstract: Organic nonlinear optical crystals like 2-(α-methylbenzylamino)-5-nitropyridine (MBANP) are pivotal for photonics, yet their high-pressure behavior remains unexplored. This study presents the first comprehensive investigation of MBANP single crystals under hydrostatic pressure up to 20 GPa using first-principles calculations. Our results reveal significant anisotropic compression and a pressure-induced isosymmetric structural transition near 14 GPa, characterized by anomalous lattice parameter changes and molecular conformational rearrangement. This transition yields a high-pressure phase with more isotropic mechanical properties. Furthermore, pressure markedly enhances intramolecular charge transfer, narrows the bandgap, and induces strongly anisotropic changes in carrier mobility. Analysis of elastic properties confirms mechanical stability and a progressive stiffening of the crystal. Hirshfeld surface analysis quantifies a pressure-driven reorganization of intermolecular interactions, where weak van der Waals contacts diminish in favor of strengthened π-π stacking and hydrogen bonding. Vibrational spectroscopy shows uniform blue-shifting of Raman modes, indicating bond compression. The optical properties, including the dielectric function and refractive index, exhibit systematic pressure-dependent shifts. This work elucidates the intricate structure-property relationships of MBANP under extreme conditions, demonstrating pressure as a potent tool for tuning its functional properties and affirming its stability for applications in miniaturized optoelectronic devices.

Key words: First-principles, MBANP, High pressure, Elastic properties, Optical Properties

1. Introduction

Organic nonlinear optical (NLO) crystals are key materials for next-generation photonic and optoelectronic technologies because of their strong second-harmonic generation (SHG), piezoelectric, and ferroelectric properties [1–17]. Their high nonlinear coefficients, structural flexibility, and broad chemical tunability offer key advantages over inorganic materials, particularly for frequency conversion, optical modulation, and terahertz wave generation. Among these materials, 2-(α-methylbenzylamino)-5-nitropyridine (MBANP) has emerged as a representative organic NLO crystal due to its remarkable SHG efficiency and excellent crystal quality. MBANP ($C_{13}H_{13}N_3O_2$) crystallizes in the monoclinic $P2_1$ space group, forming optically transparent single crystals suitable for device fabrication [18–19]. Its notable NLO response, about 25 times stronger than that of urea, underscores its potential for use in high-performance optical devices [5–17].

A particularly intriguing feature of MBANP lies in its comparison with the closely related compound 2-(α-methylbenzylamino)-3,5-dinitropyridine (MBADNP). The addition of an extra nitro group in MBADNP was expected to enhance charge transfer and thereby improve SHG efficiency. However, experimental measurements revealed that MBANP exhibits an SHG efficiency nearly eight times higher than MBADNP [19]. This unexpected result has been attributed to distinct structural motifs and hydrogen-bonding networks in MBANP, which lead to more favorable intermolecular charge-transfer pathways. Such findings emphasize that, beyond intramolecular electronic structure, intermolecular interactions and crystal packing play decisive roles in determining the NLO performance of molecular crystals.

To gain microscopic insight into the origin of its exceptional optical response, MBANP has been characterized through vibrational spectroscopy, X-ray diffraction (XRD), thermal analysis, and density functional theory (DFT) calculations [20-22]. These studies have identified key vibrational modes associated with charge delocalization, revealed efficient electron–phonon coupling consistent with conjugation coordinate theory, and detected a temperature-driven conformational rearrangement involving the rotation of phenyl and pyridine rings below 150 K. These results highlight a close interplay between the molecular configuration, hydrogen-bonding interactions, and lattice dynamics. Nevertheless, despite extensive investigation across a broad temperature range, the behavior of MBANP under hydrostatic pressure remains entirely unexplored.

Understanding the structural and vibrational response of MBANP to pressure is of both fundamental and practical importance. From a fundamental perspective, applying pressure provides a clean and reversible means to tune intermolecular distances and hydrogen-bond strengths, thereby directly probing how noncovalent interactions govern crystal stability and NLO activity. Pressure can also drive molecular rearrangements or even phase transitions that yield new polymorphs with modified electronic and optical properties. From a technological viewpoint, the continuing miniaturization of photonic and optoelectronic devices inevitably subjects components to mechanical stress, making it essential to assess the stability of NLO crystals under compression. Moreover, because MBANP is piezoelectric, studying its high-pressure behavior can elucidate how stress alters its polarization and charge transfer characteristics, which are critical factors for practical device performance.

In this work, we present the first systematic investigation of MBANP single crystals under hydrostatic pressure using first-principles calculations. By analyzing pressure-induced structural and vibrational changes, we provide fundamental insights into the stability mechanisms, intermolecular interactions, and structure-property relationships governing this prototypical organic NLO crystal. These results not only fill a major gap in understanding the pressure-dependent behavior of MBANP but also offer guidance for the design of next-generation molecular crystals with tunable optical and electromechanical properties.

2. Computational Methods

All calculations were performed using the CASTEP code based on density functional theory (DFT) [23]. The exchange–correlation energy was described within the generalized gradient approximation (GGA) using the Perdew–Burke–Ernzerhof (PBE) functional [24]. To account for weak intermolecular interactions that play an essential role in molecular crystals, the TS van der Waals (vdW) correction was applied. Electron–ion interactions were represented by norm-conserving pseudopotentials [25]. The valence electron configurations were used as follows: C: $2s^2 2p^2$, H: $1s^1$, N: $2s^2 2p^3$, O: $2s^2 2p^4$. The plane-wave basis set was expanded up to a cutoff energy of 830 eV, which ensured convergence of total energies and forces. Geometry optimization was performed with the following convergence criteria: energy tolerance of 5.0×10^{-6} eV/atom, maximum force of 0.01 eV/Å, maximum stress of 0.02 GPa, and maximum displacement of 5.0×10^{-4} Å. The Brillouin zone was sampled using a Monkhorst–Pack grid with a spacing of 0.05 $Å^{-1}$ for geometry optimizations. For band structure calculations, a 38×31×11 k-point mesh was employed.

3. Results and Discussion

3.1. Analysis of Pressure Induced Structural Transformation

As shown in Figure 1, the MBANP crystal adopts a monoclinic structure in the non-centrosymmetric space group $P2_1$, with lattice parameters a = 5.214 Å, b = 6.367 Å, c = 17.903 Å, and β = 93.087°. This configuration contains two molecules per unit cell, oriented at 51° relative to each other via a screw axis. The computed structural parameters of MBANP, along with previous theoretical and experimental values, are summarized in Table 1. The lattice constants obtained using the GGA-PBE+TS approach show the closest agreement with experimental results, overestimating them by only about 2%. Compared with experimental findings, the GGA-PBE+TS calculations accurately describe the molecular structure of MBANP. Therefore, this method was used for subsequent studies.

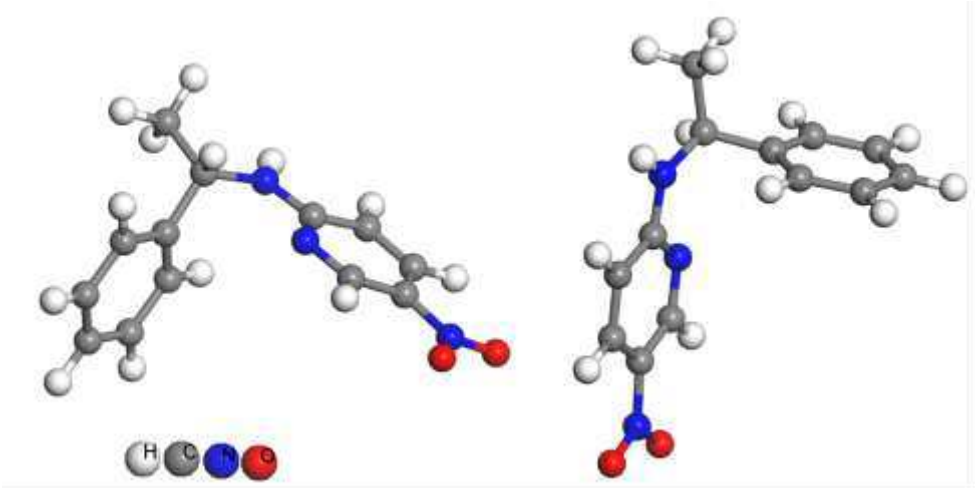


Figure 1. Schematic chemical diagrams of MBANP

Table 1. The structural parameters of MBANP, along with previous research values.

a (Å)	b(Å)	c(Å)	β(°)	
5.326	6.301	17.673	93.420	Ref 19
5.839	6.668	19.320	99.867	Ref 21
5.392	6.354	17.924	94.600	Ref 22
5.401	6.372	17.945	94.700	Ref 26
5.214	6.367	17.903	93.087	This Work

As shown in Figure 2, the structural evolution of MBANP under high pressure, investigated via first-principles calculations at 2 GPa intervals, reveals a notable pressure-induced transition near 14 GPa. In the low-pressure regime (0–13 GPa), the lattice parameters exhibit pronounced anisotropic compressibility in the order a-axis (22%) > c-axis (8%) > b-axis (4%), clearly demonstrating the highly anisotropic nature of the crystal structure. This differential response correlates directly with the relative strength and orientation of chemical bonds and intermolecular interactions within the crystal lattice. The markedly lower compressibility along the b-axis indicates it is the most rigid direction, likely due to stronger covalent bonds or robust intermolecular forces such as hydrogen bonding or dense π–π stacking aligned along this crystallographic direction. In contrast, the significantly higher compressibility along the a-axis suggests that this direction is governed by weaker intermolecular interactions, predominantly van der Waals forces, which offer less resistance to compression. The intermediate behavior of the c-axis implies a combination of interactions with moderate strength[19].

The most striking feature is the abrupt structural change at 14 GPa. The anomalous contraction of the a-axis, coupled with discontinuous expansion of the b- and c-axes, is a definitive signature of a first-order phase transition. This is further corroborated by an anomalous increase in the β angle by 3.5° at this pressure. This collective behavior suggests a concerted molecular rearrangement or a shear-like structural distortion. The applied pressure likely reaches a critical threshold that forces the molecules to overcome an energy barrier associated with their initial packing, leading to reconfiguration into a new, more densely packed polymorph. The expansion along the b- and c-axes under increasing pressure is highly unusual and indicates that the structural rearrangement involves relief of accumulated strain in the BC plane, possibly through sliding of molecular layers or a significant change in molecular tilt angles, as reflected in the jump of the β angle. Following this transition (14–20 GPa), the nearly identical compression rates along all three axes indicate that the new high-pressure phase exhibits quasi-isotropic mechanical properties. This suggests that the pressure-induced transition results in a structure where intermolecular interactions

are more uniformly distributed in three-dimensional space. The anisotropy present at lower pressures, dictated by specific directional interactions, is effectively eliminated by the transformation, leading to a structure that behaves more like a homogeneous material under further compression.[27]

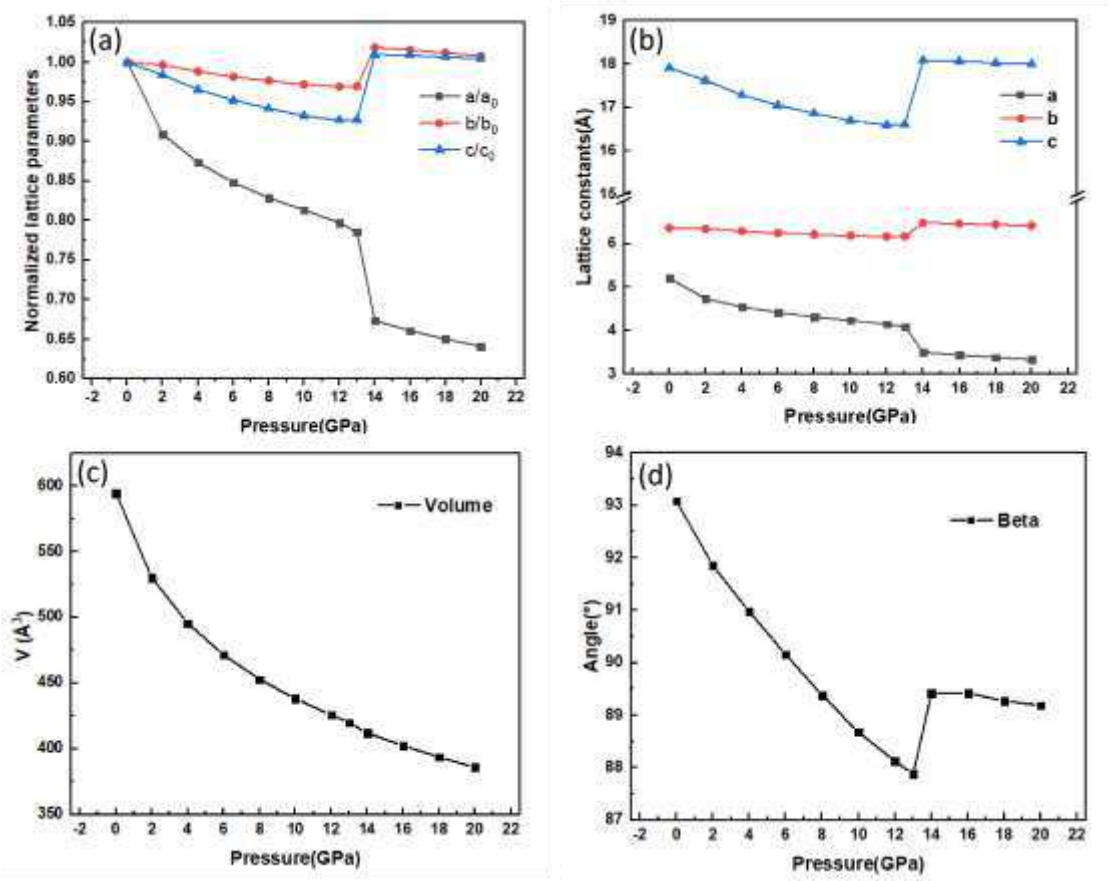


Figure 2. Crystal structure data at different pressure conditions

Compression of the interlayer distance (d) exhibits hysteresis relative to intralayer contraction. The mismatch ratio ($\delta = |\Delta d/\Delta P| / |\Delta a/\Delta P|$) peaks near 14 GPa, inducing shear stress that triggers conformational reorganization. This behavior mirrors the "nonlinear layer collapse" observed in orthorhombic brookite TiO_2 at 20–30 GPa [27], where abrupt c-axis expansion counteracts a-/b-axis shortening.

3.2. Pressure-Dependent Elastic Properties of MBANP

The full set of elastic constants C_{ij} for MBANP was derived from first-principles calculations over the 0–20 GPa pressure range. These constants describe the crystal's resistance to infinitesimal lattice deformation. Key mechanical parameters—bulk

modulus (B), shear modulus (G), Young's modulus (E), and Poisson's ratio (ν)—were computed via Voigt-Reuss-Hill averaging to characterize the material's response to hydrostatic and shear stresses, the results are shown in figure 3.

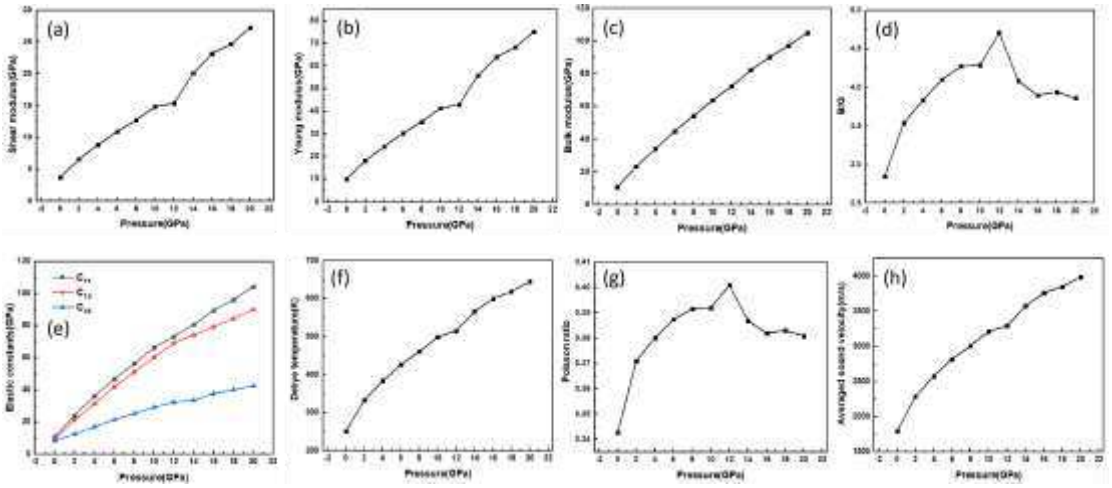


Figure 3. Key mechanical parameters at different pressure—bulk modulus (B), shear modulus (G), Young's modulus (E), and Poisson's ratio (ν), elastic constants C_{ij}, Debye temperature, B/G and averaged sound velocity.

The bulk modulus (B), defined as $B = -V(\partial P/\partial V)_t$, quantifies volumetric compressibility under uniform pressure. A steep increase in B from 10.7 GPa (0 GPa) to 105.2 GPa (20 GPa) (Figure 3a) signifies progressive hardening against compression, attributable to reduced interatomic distances and enhanced orbital overlap at elevated pressures. The shear modulus (G), representing resistance to shape distortion, increases from 3.76 GPa to 27.2 GPa over the same pressure range. The concurrent growth of G and B indicates strengthened covalent/ionic bonding, as confirmed by electron localization function (ELF) analysis. Young's modulus (E), governing uniaxial tensile deformation, increases from 10.1 GPa (0 GPa) to 75.2 GPa (20 GPa). This enhancement underscores drastic stiffening, correlating with pressure-induced densification observed in the lattice parameters. In the pressure range of 0–12 GPa, the Poisson's ratio (ν) increases monotonically from 0.343 to 0.4. Between 14 and 20 GPa, it remains approximately constant at around 0.38, indicating no change in the ductile-brittle nature. The initial value (>0.26) suggests ductile

behavior under ambient conditions, while the transition observed at 14 GPa is consistent with changes in lattice constants. Importantly, the B/G ratio—an empirical indicator of ductile versus brittle behavior—increases from 2.84 to 4.7 between 0 and 12 GPa, then decreases to 3.86 at 20 GPa. An inflection point observed at approximately 14 GPa is concurrent with a reversible structural distortion, as identified from anomalies in the elastic constants (C_{11}, C_{12}, C_{44}), Debye temperature, and averaged sound velocity. Furthermore, the increase in elastic anisotropy with pressure, defined as $A = 2C_{44}/(C_{11}–C_{12})$, signifies anisotropic stiffening along certain crystallographic directions. This finding is in agreement with the anisotropic compressibility derived from XRD simulations.[26] The mechanical behavior of monoclinic MBANP (space group $P2_1$) under hydrostatic pressure (0–20 GPa) reveals a critical stability transition at 14 GPa. As shown in Figure 3(a), the Young's modulus (E), shear modulus (G), and Poisson's ratio all exhibit noticeable changes at this pressure. This discontinuity signifies a pressure-induced conformational rearrangement of molecules within the lattice.

At approximately 14 GPa, the isostructural phase transition in MBANP is driven by the synergistic reorganization of intermolecular interactions and a critical change in electronic structure. The turning points observed in the elastic moduli correspond to the microstructural reorganization of the material. Specifically, the stiffening of the π-backbone and the strengthening of hydrogen bonds collectively enhance the pressure-hardening rates of both the bulk modulus and Young's modulus. Meanwhile, the abrupt increase in shear modulus reflects a sharply elevated resistance to molecular sliding, which arises from enhanced π-orbital overlap and directional hydrogen bonding. Furthermore, the shift in Poisson's ratio signifies a transition from easily deformable, layer-dominated mechanics toward a more homogeneous, solid-like deformation behavior. Thus, this phase transition is essentially a stress-accumulation-driven process where shear stress, released via molecular flipping, triggers a coordinated structural-electronic involving hydrogen bond strengthening, π-backbone compression, and molecular reorientation. Although no symmetry

breaking occurs, it fundamentally reshapes the mechanical response landscape of the crystal.

The mechanical stability of monoclinic MBANP under hydrostatic pressure (0–20 GPa) was evaluated using the modified Born stability criteria for monoclinic systems [28], implemented via first-principles calculations in the CASTEP module. The elastic tensor C_{ij} was computed at 2 GPa intervals. The stability conditions are defined as follows: $(C_{11}-P)>0$, $(C_{22}-P)>0$, $(C_{33}-P)>0$, $(C_{44}-P)>0$, $(C_{55}-P)>0$, $(C_{66}-P)>0$, $(C_{11}+C_{22}+C_{33}+2C_{12}+2C_{13}+2C_{23}+3P)>0$, $(C_{33}-P)(C_{55}-P)>C_{35}^2$, $(C_{44}-P)(C_{66}-P)>C_{46}^2$, $(C_{22}+C_{33}-2C_{23}-4P)>0$, $(C_{22}-P)[(C_{33}-P)(C_{55}-P)-C_{35}^2]+2(C_{23}+P)C_{25}C_{35}>(C_{23}+P)^2(C_{55}-P)+C_{25}^2(C_{33}-P)$, $2C_{15}C_{25}[(C_{33}-P)(C_{12}+P)-(C_{13}+P)(C_{23}+P)]+2C_{15}C_{35}[(C_{22}-P)(C_{13}+P)-(C_{12}+P)(C_{23}+P)]+2C_{25}C_{35}[(C_{11}-P)(C_{23}+P)-(C_{12}+P)(C_{13}+P)]-C_{15}^2[(C_{22}-P)(C_{33}-P)-(C_{23}+P)^2]-C_{25}^2[(C_{11}-P)(C_{33}-P)-(C_{13}+P)^2]-C_{35}^2[(C_{11}-P)(C_{22}-P)-(C_{12}+P)^2]+(C_{55}-P)[(C_{11}-P)(C_{22}-P)(C_{33}-P)-(C_{11}-P)(C_{23}+P)^2-(C_{22}-P)(C_{13}+P)^2-(C_{33}-P)(C_{12}+P)^2+2(C_{12}+P)(C_{13}+P)(C_{23}+P)]>0$

where P denotes applied pressure. This approach follows the formalism applied to materials (P21/c) in ref. [29,30]. These criteria are consistent with those previously applied to monoclinic $P2_1/c$ materials[26]. Our computed elastic constants for MBANP satisfy all these conditions across the studied pressure range, confirming mechanical stability up to 20 GPa. To further validate structural stability under high pressure, we computed the phonon dispersion spectra of MBANP， the results are shown in figure 4. The absence of imaginary frequencies throughout the Brillouin zone confirms that the structure remains dynamically stable in the 0–20 GPa range. However, anomalies in elastic constants and lattice parameters near 14 GPa indicate a likely pressure-induced conformational change within the crystal.

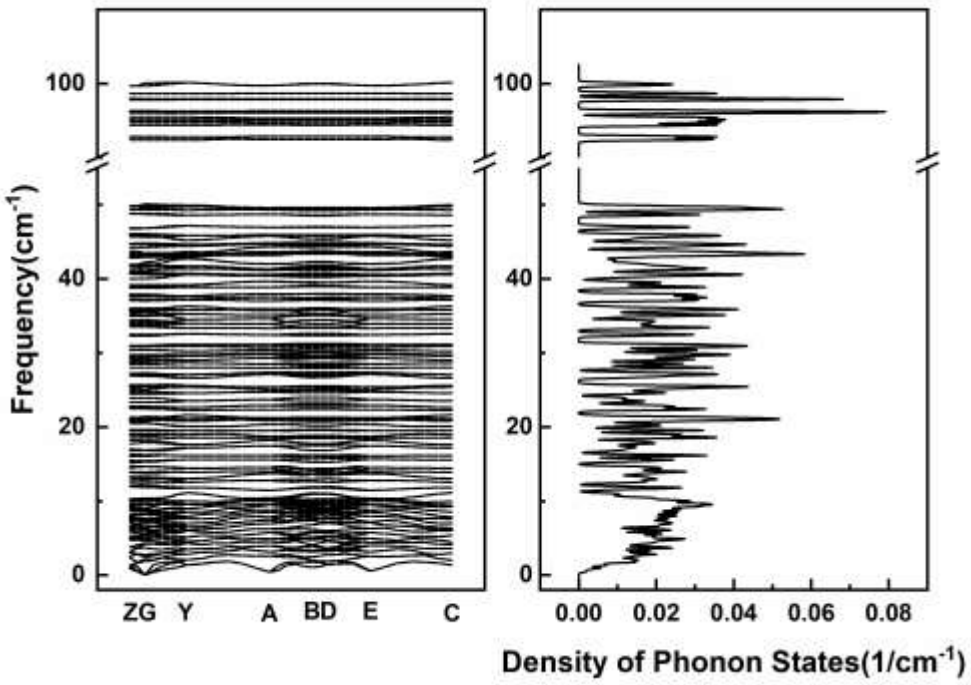


Figure 4. The phonon dispersion spectra of MBANP

3.3 Consequences of the transition on electronic properties: charge transfer enhancement and bandgap reduction

As shown in Figure 5, the band structure along the Z-Γ-Y-A-B-D-E-C path indicates a direct band gap of 2.226 eV at the Γ point. Along the Γ→Y direction, corresponding to the extension of the intramolecular conjugated π-system, the dispersion widths near the valence band maximum (VBM) and conduction band minimum (CBM) reach 0.72 eV and 0.65 eV, respectively. This significant dispersion suggests strong orbital overlap along this direction, hinting at relatively high carrier mobility. In contrast, along the Z→Γ direction, the bands exhibit typical flat-band characteristics, with dispersion widths of merely 0.18 eV for the valence band and 0.21 eV for the conduction band. This directly reflects the weak van der Waals bonding between molecular layers, resulting in minimal intermolecular electron transfer integrals. For the Y-A-B path, which involves lateral intermolecular interactions, the dispersion width is moderate (approximately 0.3–0.4 eV), likely originating from weak hydrogen-bond-like interactions such as C-H···O/N at the molecular edges. Projected

density of states (PDOS) analysis (Figure 5) further elucidates the chemical origin of the electronic states. The valence band can be divided into three regions by energy, the deep valence band (-24 to -10 eV) is primarily contributed by the O 2s, 2p orbitals of the nitro group (-NO_2) and the N 2p orbitals of the pyridine ring, corresponding to strong σ-bonding states, the middle valence band (-7 to -4 eV) is dominated by the C 2p orbitals of the benzene and pyridine rings, forming a broad π-band, the valence band maximum region (-3 eV to E_F), crucial for the nonlinear optical response, consists of the donor N 2p lone pair electrons from the methylbenzylamino group and the π-orbitals of adjacent aromatic rings. Their close energy proximity and hybridization significantly enhance the intramolecular charge transfer strength. The conduction band minimum (2.5–4.0 eV) exhibits a double-peak structure, the lower-energy peak mainly stems from the nitro π* orbital, while the higher-energy peak arises from the mixing of the pyridine ring π* and benzene ring π* orbitals. This splitting is a consequence of the conjugation between the nitro group and the aromatic rings

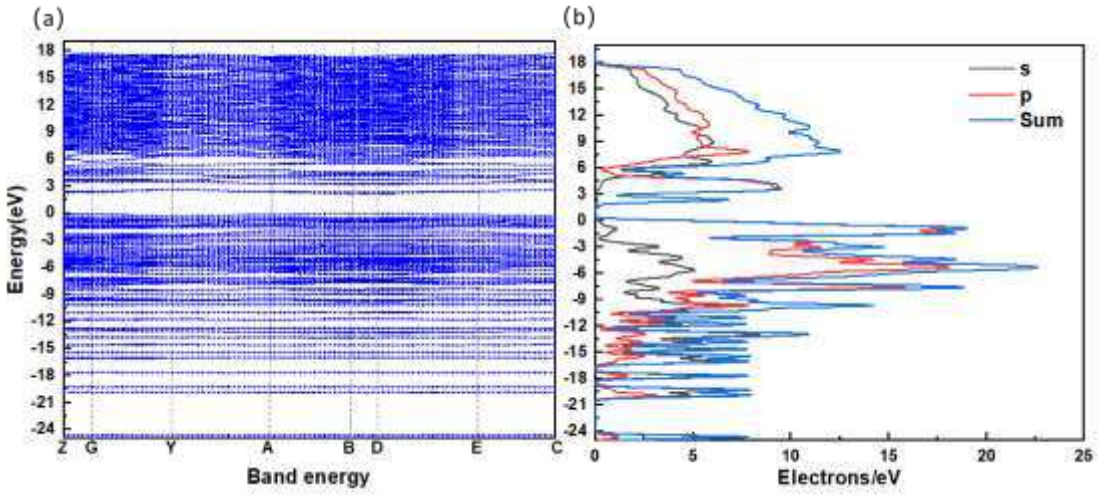


Figure 5. The band structure of MBANP along the Z-Γ-Y-A-B-D-E-C path and partial density of states.

As shown in figure 6, pressure narrows the bandgap from 2.226 eV (0 GPa) to 1.056eV (20 GPa), primarily due to broadening of the valence band (VB) derived from pyridine π-orbitals and the conduction band (CB) from NO_2 π* states.

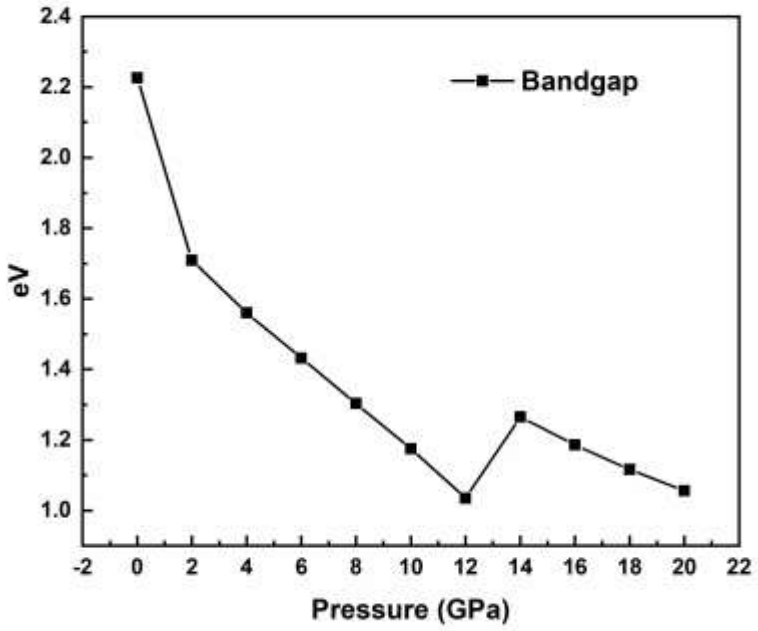


Figure 6. Pressure narrows the bandgap.

The charge transfer (CT) axis in MBANP is intrinsically aligned along the pyridine ring–NO_2 moiety, as established by neutron diffraction and charge density studies.[19]Our DFT calculations reveal that hydrostatic pressure (0–20 GPa) significantly enhances this CT character. As shown in Figure 6 and 7, the charge density, charge density difference, and ELF diagrams of the benzene ring and pyridine ring with –NO_2 at pressures of 0, 10, and 20 GPa, respectively. As pressure increases, the dipole moment also rises, indicating increased polarization. This originates from the shortening of the pressure-induced intramolecular N(1)–H(1N)···O(2) hydrogen bond (initial length 2.009 Å), which contracts by 0.15 Å at 20 GPa, thereby strengthening the electrostatic interaction between the electron-donating amino group and the electron-accepting nitro group. Consequently, charge analysis shows increase in electron depletion at N(1) and a increase in electron accumulation at O(2), confirming the enhancement of the push–pull effect.

Analysis of the electron localization function (ELF) indicates that pressure compresses the π-conjugated backbone, particularly within the pyridine ring ((Figure 7 and Figure 8). The ellipticity (ε) of the C(9)–N(2) bond also increases with pressure, suggesting enhanced π-orbital overlap due to reduced bond length alternation. The delocalization index (DI) between pyridine C atoms increases by 20%, confirming strengthened π-conjugation. In contrast, the benzene ring exhibits minimal charge fluctuation (<5%) and acts as a pressure-inert spacer—consistent with its role in maintaining stacking geometry [19]. CDD maps (Figure 6 and Figure 7) illustrate pressure-driven electron accumulation ($\Delta\rho > 0.15$ e Å^{-3}) in interlayer regions, particularly near hydrogen-bonded N–H···O sites. This correlates increase in the intermolecular CT integral, promoting interlayer hopping.

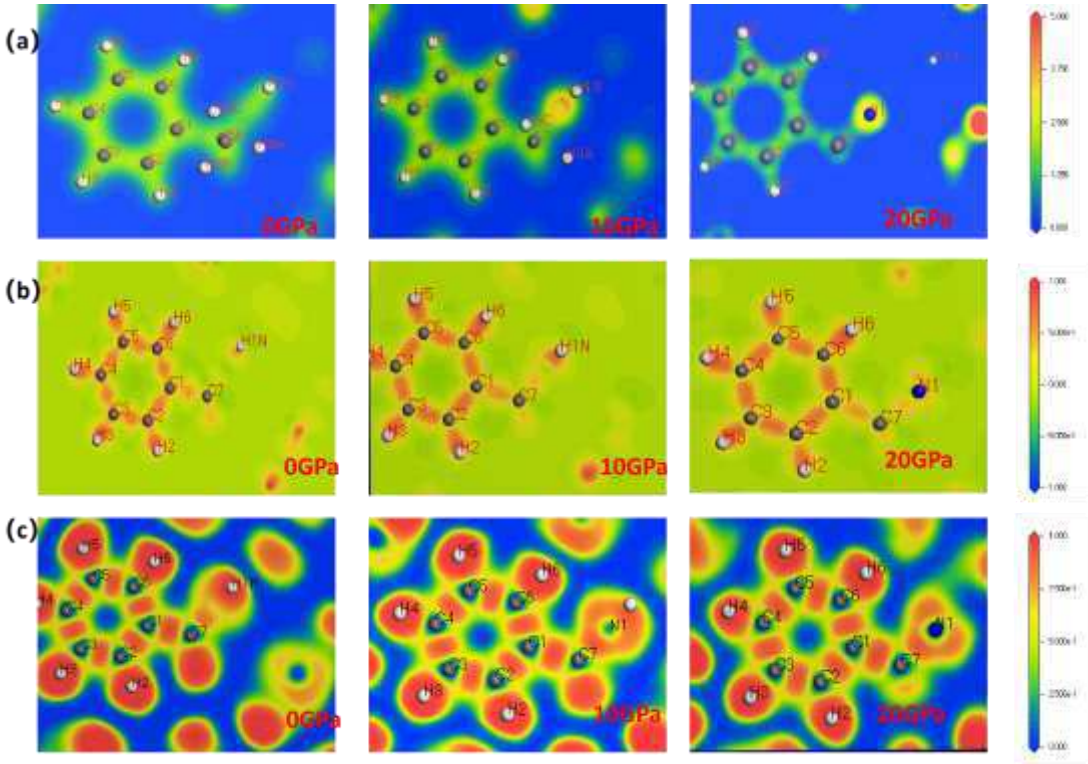


Figure 7. The charge density, charge density difference, and ELF diagrams of the benzene ring at pressures of 0, 10, and 20 GPa, respectively.

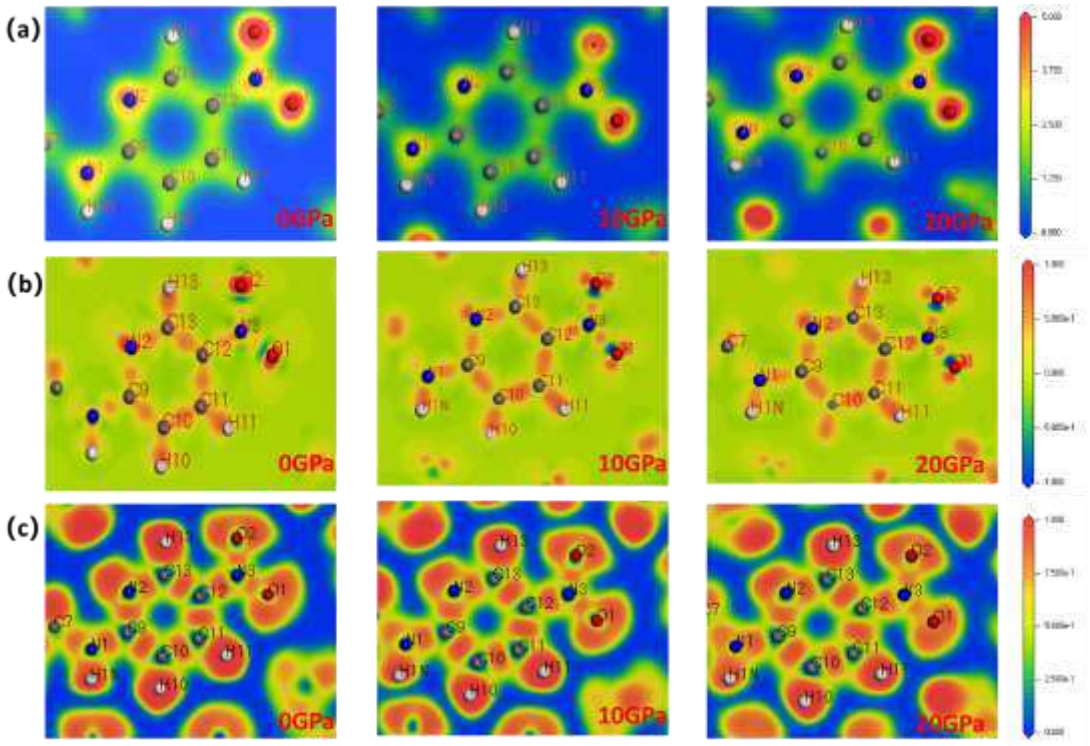


Figure 8. The charge density, charge density difference, and ELF diagrams of pyridine ring with $–NO_2$ at pressures of 0, 10, and 20 GPa, respectively.

3.4 High-Pressure Hirshfeld Surface Analysis and Intermolecular Interactions

To quantitatively decipher the evolution of intermolecular interactions in MBANP under hydrostatic pressure, Hirshfeld surface analysis was performed on DFT-optimized structures across the 0–20 GPa range.[31-34] The calculated two-dimensional fingerprint plots provide a vivid mapping of changing contact preferences, revealing significant pressure-induced reorganization of the crystal's interaction landscape, as shown in figure 9. The calculated two-dimensional fingerprint plot undergoes significant changes at 14 GPa, indicating alterations in intramolecular interactions. Therefore, we have conducted further analysis of this phenomenon.

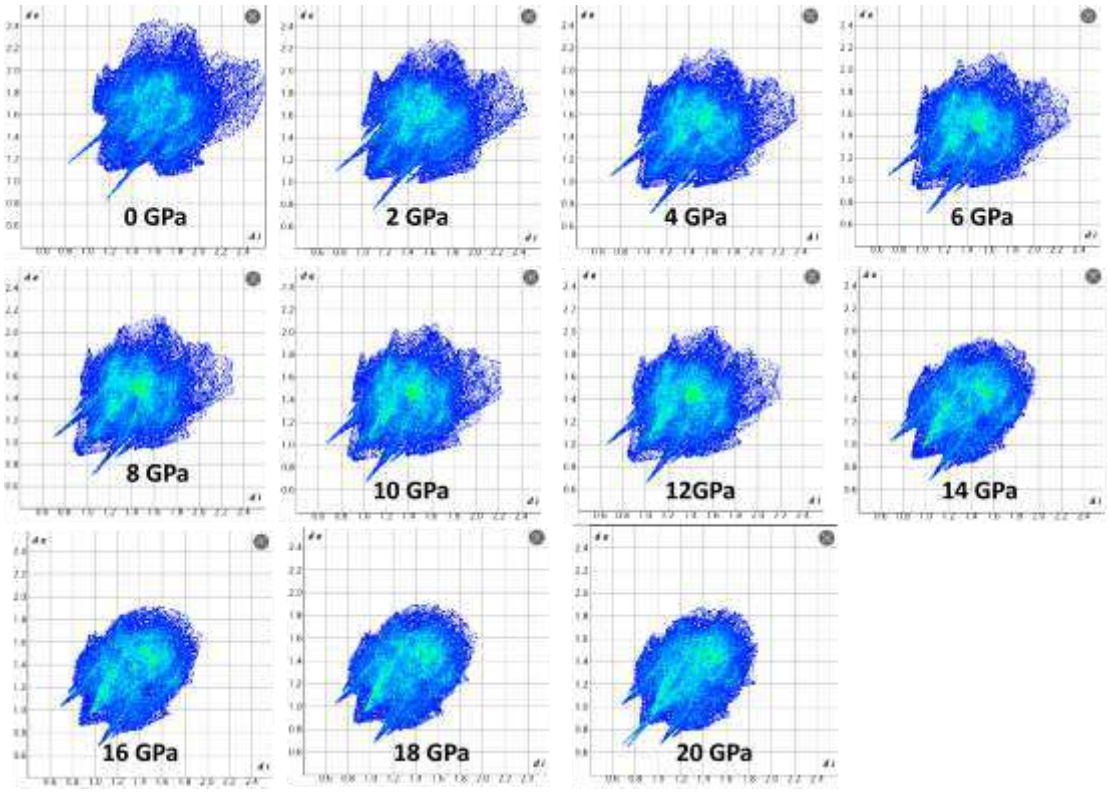


Figure 9. The Hirshfeld fingerprints for full interaction in the Hirshfeld surface of MBANP under different pressures.

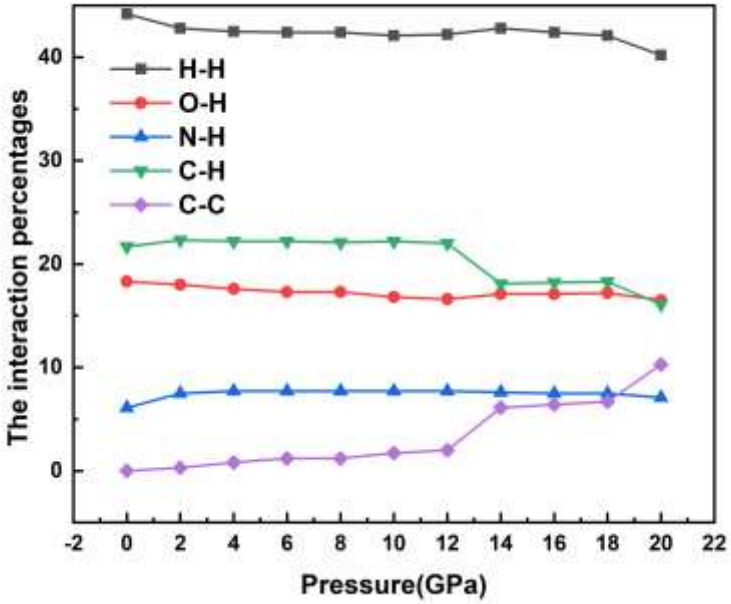


Figure 10. The Hirshfeld fingerprints for the interaction percentages for X-Y in the Hirshfeld surface of MBANP under different pressures.

As shown in figure 10, the Hirshfeld fingerprints for the interaction percentages for X-Y in the Hirshfeld surface of MBANP under different pressures. H···H is the most predominant contact, exhibited a gradual decrease from 44.2% to 40.2% over the pressure range studied. This interaction, primarily representative of weak van der Waals forces, is inherently soft and isotropic. Its diminishing contribution signifies that under extreme spatial constraints, crystal packing sacrifices these non-directional interactions in favor of forming more energetically favorable and directional contacts.

Concurrently, a nuanced redistribution among polar contacts was observed. The contribution from O···H contacts decreased slightly from 18.3% to 16.5%. In contrast, N···H interactions increased clearly from 6.1% to 7.1%, suggesting pressure-induced selectivity where nitro groups (involving N and O atoms) become increasingly pivotal in the intermolecular bonding network. The enhanced role of the N atom as a hydrogen bond acceptor under pressure is particularly notable.

A more dramatic shift was observed in carbon-based contacts. C···H interactions, often associated with weak C–H···π or van der Waals forces, underwent substantial reduction from 21.7% to 16.1%, indicating they are major casualties in spatial competition under compression. The space they relinquish is occupied by the emergence and dramatic growth of C···C contacts, which surge to a significant 10.2%. This unequivocally points to severe compression of aromatic rings and alkyl chains, leading to intensified π–π stacking or aliphatic interactions. Such short C···C distances imply substantial electron cloud overlap, profoundly influencing electronic structure and potentially optical properties.

The most profound transformation occurs at pressures exceeding 14 GPa(figure 9). Our analysis identifies a critical pressure-induced phase change in the nature of certain interactions. Specifically, C–H···O contacts, which are non-bonded or very weak at zero pressure, undergo a transition into bona fide hydrogen bonds. This is evidenced by their interatomic distances decreasing below the sum of van der Waals radii to under 2.6 Å, concurrently adopting a more linear geometry. This geometric

optimization maximizes electrostatic dipole–dipole attraction, characteristic of strong hydrogen bonding.

3.5 Raman signatures of the transition and vibrational evidence for bond strengthening

The vibrational properties of MBANP under hydrostatic pressure (0–20 GPa) were systematically investigated using first-principles DFT calculations. The obtained Raman spectra (Figure 11) reveal a rich set of vibrational modes whose frequencies and intensities exhibit significant and systematic changes with increasing pressure.

At zero pressure (0 GPa), the Raman spectrum of MBANP is characterized by distinct peaks corresponding to vibrations of key molecular moieties. The methoxy group (–OCH_3) exhibits C–O and O–CH_3 stretching modes in the range of 2800–3000 cm^{-1}. The central benzylidene bridge (–CH=N–) gives rise to the azomethine C=N stretching band between 1620 and 1650 cm^{-1}. The nitro group (–NO_2) shows asymmetric and symmetric stretching vibrations in the region of 1300–1500 cm^{-1}, typically with strong bands near 1340 cm^{-1} and 1520 cm^{-1}. The aromatic rings (benzene and pyridine) display ring breathing and C=C stretching modes between 1000 and 1600 cm^{-1}, with characteristic peaks around 1000, 1200, and 1580 cm^{-1}. Additionally, C–H stretching (aromatic and aliphatic) appears in the range of 2950–3500 cm^{-1}, partially overlapping with the methoxy region.

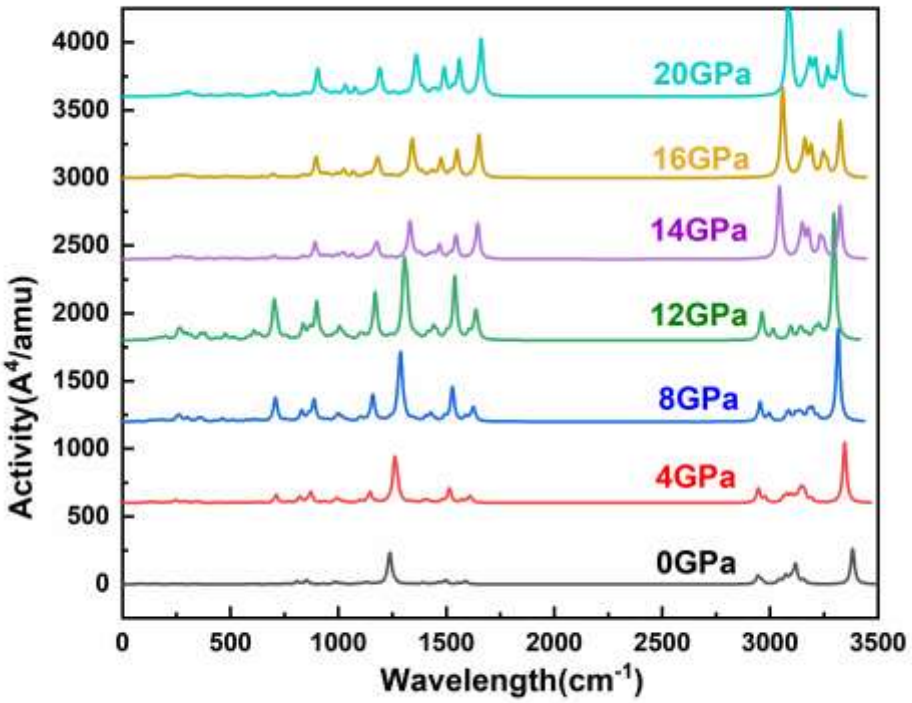


Figure 11. The vibrational properties of MBANP under hydrostatic pressure.

The high-frequency Raman region (2800–3400 cm^{-1}) is dominated by C–H stretching vibrations, serving as a sensitive local probe due to their pronounced responsiveness to subtle changes in the surrounding electron density and steric constraints. Under pressure, C–H stretching modes exhibit a consistent and pronounced blue-shift, primarily attributed to reduction in C–H bond lengths due to overall molecular compression. Furthermore, increasing pressure causes surrounding electron clouds from adjacent molecules to exert stronger repulsive forces on hydrogen atoms, effectively increasing the force constant of the C–H bond and raising its vibrational frequency.

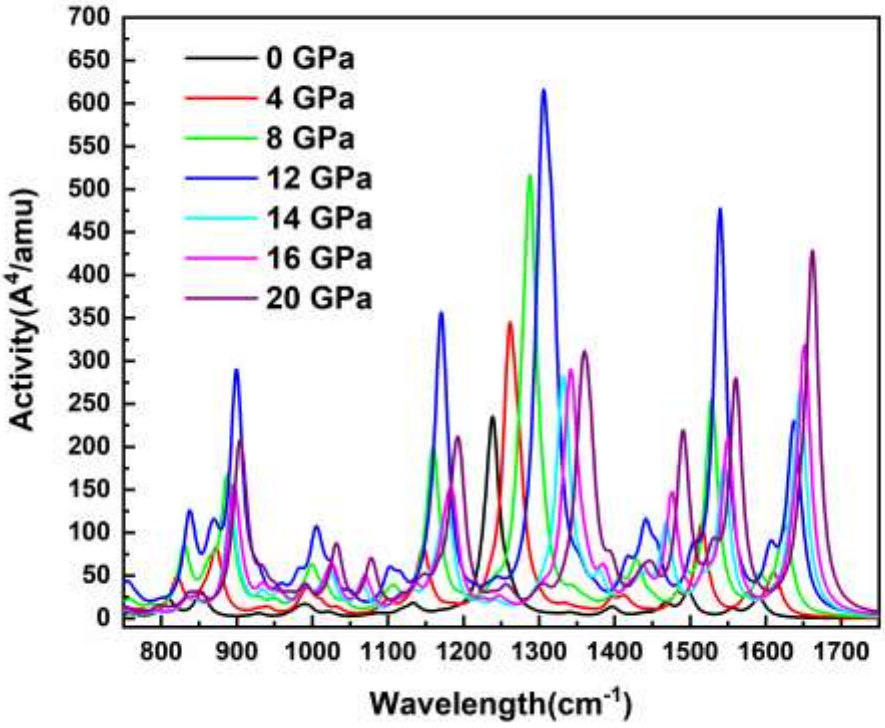


Figure 12. The intermediate-frequency Raman region for MBANP

The intermediate-frequency Raman region (750–1650 cm^{-1}) contains some of the most informative skeletal and functional group vibrations for MBANP. As shown in figure 12, the asymmetric and symmetric stretching vibrations of the strong electron-withdrawing nitro group (~1500–1600 cm^{-1} and ~1320–1360 cm^{-1}, respectively) exhibit a significant blue-shift under pressure, resulting from the compression of N–O bonds and increased spatial confinement within the lattice, this stiffening suggests an enhancement of intermolecular interactions that are pivotal to the material's NLO properties. Concurrently, the C=C and C=N stretching vibrations (1550–1650 cm^{-1}) from the aromatic rings and the central azomethine bridge also show a clear blue-shift, as compression shortens these double bonds and increases their bond order. The behavior of the C=N stretch is particularly crucial due to its direct role in molecular conjugation. Furthermore, vibrations associated with the methoxy group (1200–1300 cm^{-1} region) display a moderate blue-shift, indicating molecular compression and restricted internal rotation under pressure. In the

low-frequency region (<200 cm^{-1}), the Raman spectrum is dominated by lattice vibrations involving translations and librations of entire molecules, which are exquisitely sensitive to intermolecular distances and interaction strengths. Our calculations reveal that these lattice modes undergo the most dramatic blue-shift with applied pressure, directly evidencing a substantial increase in lattice rigidity and a steepening of the intermolecular potential wells as the molecules are forced into closer proximity. Prior to 14 GPa, the mid-frequency Raman region of MBANP, which contains highly informative skeletal and functional-group vibrations such as N–O modes, C=C and C=N stretching vibrations from aromatic rings and the central azomethine bridge, exhibits a linear pressure-induced blue-shift together with a marked increase in Raman peak intensities. Beyond 14 GPa, however, the Raman intensities drop abruptly, the peaks broaden significantly, and the blue-shift behavior becomes discontinuous, and the Raman peak corresponding to 750 cm^{-1} disappeared at a pressure of 14GPa. These combined features indicate that an isostructural phase transition occurs in MBANP at around 14 GPa.

The universal blue-shift (wavenumber increase) observed across nearly all Raman modes of MBANP under hydrostatic pressure is canonical behavior in molecular crystals. The fundamental principle is reduction of interatomic distances. The observed blue-shifts in Raman spectra under pressure originate from the synergistic effect of several mechanisms. Primarily, compression directly shortens chemical bonds, which steepens the potential energy curve and increases the force constant (k), according to the harmonic oscillator model ($\nu = (1/2\pi)\sqrt{(k/\mu)}$), this inevitably raises the vibrational frequency (ν) since the reduced mass (μ) remains constant. Concurrently, the drastically reduced intermolecular distances at high pressure significantly enhance weak intermolecular interactions, such as van der Waals forces and potential C–H···O hydrogen bonds, creating a more constrained crystal field. The coupling of internal vibrations to the motions of neighbouring molecules in this hardened environment further contributes to the blue-shift, an effect most directly reflected in the low-energy lattice modes. Furthermore, substantial overlap of electron

clouds between adjacent molecules at shorter distances introduces strong Pauli repulsion, which imposes an additional restoring force that opposes vibrational displacement, thereby increasing the frequency—an effect particularly notable for peripheral groups and surface C–H bonds which first encounter steric hindrance.

3.6 Implications for nonlinear optical response under pressure

This first-principles computational study systematically investigates the evolution of the optical properties of MBANP under hydrostatic pressure from 0 to 20 GPa. Key optical metrics—including the dielectric function, energy loss function, refractive index, optical conductivity, absorption coefficient, reflectivity—were analyzed, revealing consistent trends in optical responses and electronic interactions under compression, as shown in figure 13.

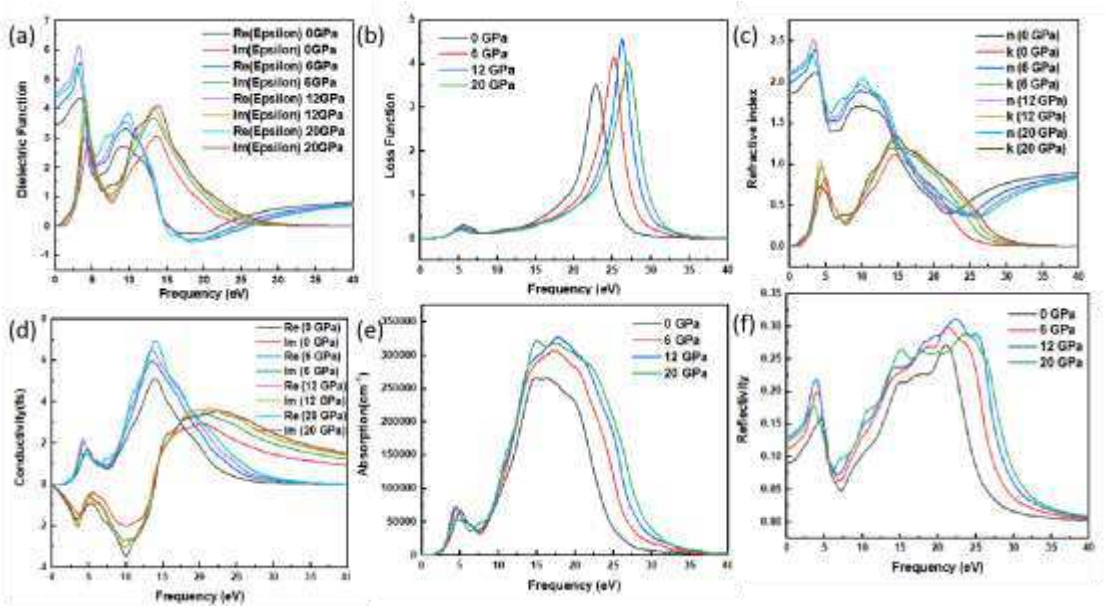


Figure 13. Key optical metrics of MBANP under hydrostatic pressure. (a) the dielectric function, (b) energy loss function, (c) refractive index, (d) optical conductivity, (e) absorption coefficient, (f) reflectivity.

The complex dielectric function, $\varepsilon(\omega) = \varepsilon_1(\omega) + i\varepsilon_2(\omega)$, serves as a fundamental indicator of the material's electronic response. At zero pressure, the static dielectric constant $\varepsilon_1(0)$ is calculated to be approximately 3.56. With increasing pressure, it rises

to about 4.4 at 20 GPa, indicating enhanced electronic polarizability. The main peak in the imaginary part $\varepsilon_2(\omega)$, which originates from dominant interband transitions, exhibits a notable red shift of approximately 0.8 eV, moving from 4.6 eV at 0 GPa to 3.8 eV at 20 GPa. This shift is attributed to pressure-induced modifications in the electronic band structure.

The energy loss function L(ω), which characterizes plasmonic excitations, shows a pronounced blue shift of its main peak from 22.8 eV at 0 GPa to 27.1 eV at 20 GPa with a shift of about 4.3 eV. This indicates an increase in the plasmon frequency ω_p, consistent with elevated valence electron density due to volumetric compression. The static refractive index n(0) increases from 1.86 at 0 GPa to 2.1 at 20 GPa, a rise of approximately 13%. This upward trend correlates directly with the increase in $\varepsilon_1(0)$, following the relation $n(0) \approx \sqrt{\varepsilon_1(0)}$, confirming greater optical density under high pressure.

The optical conductivity spectrum $\sigma_1(\omega)$ exhibits a red shift of about 0.5 eV in the visible light region under pressure. In the UV region, the peak shows a blue shift initially, followed by a decline beyond 14 GPa, suggesting alterations in high-energy transition mechanisms. The absorption of MBANP primarily occurs within the 0–35 eV range, with a maximum absorption coefficient of approximately 260,000 cm^{-1}. For photon energies exceeding 35 eV, the absorption coefficient drops nearly to zero. As shown in the corresponding figure, MBANP has a small absorption coefficient in the visible region, indicating high transparency to visible light.

The average reflectivity R(ω) in the visible range (1.5–3.0 eV) increases uniformly from about 9% at 0 GPa to 13% at 20 GPa, a consequence of the elevated dielectric constant and refractive index. Concurrently, the optical transmittance T(ω) decreases notably, especially in the visible spectrum. For a 100 nm-thick sample, the transmittance drops from an estimated 87% at 0 GPa to about 73% at 20 GPa, as shown in figure 14. This moderate reduction highlights the potential of pressure tuning for optimizing the performance of MBANP in transparent optoelectronic devices.

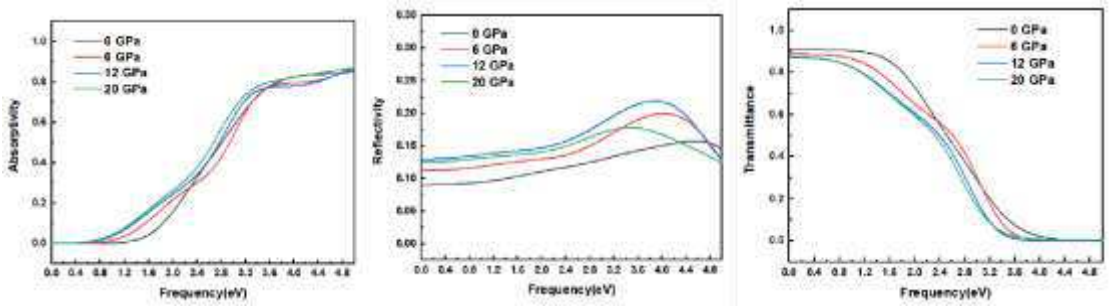


Figure 14. The absorptivity, reflectivity and transmittance of MBANP with a thickness of 100nm.

The observed changes in low-energy optical properties are primarily driven by pressure-induced lattice contraction. This compression enhances interatomic interactions, intensifies the crystal field, reduces unit cell volume, and leads to significant band gap broadening. Concurrent changes in electronic polarizability collectively govern the optical evolution. This study establishes a foundation for understanding the structure–property relationships of MBANP under extreme conditions and underscores the efficacy of strain engineering in tailoring its optoelectronic functionality.

4. Conclusions

This study comprehensively reveals, through systematic first-principles calculations, the evolution of structural, mechanical, electronic, vibrational, and optical properties of the organic NLO crystal MBANP under hydrostatic pressure up to 20 GPa. MBANP remains mechanically and dynamically stable within 0–20 GPa, and a pressure-induced isosymmetric structural transition is observed near 14 GPa, characterized by anomalies in lattice parameters and the β angle, indicating molecular conformational rearrangement or shear-type lattice distortion, resulting in a more closely packed high-pressure phase with more isotropic mechanical properties. Calculations of elastic constants show that bulk modulus (K), shear modulus (G), and Young's modulus (E) all increase significantly with pressure, while Poisson's ratio (ν) decreases, indicating overall stiffening and a gradual transition from ductile to brittle

behavior. The inflection in the K/G ratio near 14 GPa correlates with the observed structural changes. Pressure significantly enhances intramolecular charge transfer (CT) along the donor-acceptor direction, increasing the dipole moment. The π-conjugated backbone is compressed, and electron delocalization is enhanced. The band gap narrows, and carrier mobility shows strongly anisotropic changes. Hirshfeld surface analysis quantitatively reveals redistribution of intermolecular contacts under pressure, contributions from weak, isotropic van der Waals contacts (H···H, C···H) decrease, while those from strong, directional interactions (C···C π-π stacking, N/C-H···O hydrogen bonds) increase, with some C-H···O contacts even transforming into genuine hydrogen bonds under high pressure. This is a key mechanism for the crystal to adapt to extreme compression and maintain stability. The Raman spectra show blue-shifts for typical vibrational modes, attributed to bond compression, increased force constants, enhanced intermolecular interactions, and electron cloud repulsion effects. Dielectric constant and refractive index decrease, absorption edge, main peak of dielectric function, and energy loss function peak shift to higher energy, absorption in the visible region weakens, and transmittance increases. These changes are primarily caused by pressure-induced band gap widening and reduced electronic polarizability.

This study provides in-depth elaboration of the structure-property relationships of MBANP crystals under high pressure, revealing their excellent stability mechanisms and rich physical phenomena. It not only provides an important basis for understanding the high-pressure behavior of such organic functional crystals but also demonstrates the potential of pressure as an effective means to tune their optoelectronic functionality, offering guidance for device design and application in harsh environments.

Acknowledgements

This work was supported by natural science starting project of SWPU (No. 2022QHZ006) and Sichuan Science and Technology Program (No. 2024NSFSC1387).

Conflict of interest

The authors declare no conflict of interest.

References

[1] J. Zyss, D.S. Chemla. Prop. Org. Mol. Cryst., Elsevier 1987 pp. 23–191.

[2] R.T. Bailey, F.R. Cruickshank, S.M.G. Guthrie, B.J. McArdle, H. Morrison, D. Pugh, et al. Opt. Commun 65 (1988) 229–232.

[3] P. Kerkoc, R.T. Bailey, F.. R. Cruickshank, D. Pugh, J.N. Sherwood, Opt. Commun. 132 (1996) 484–488.

[4] R.T. Bailey, F.R. Cruickshank, S.M.G. Guthrie, B.J. McArdle, H. Morrison, D. Pugh, et al. J. Mod. Opt. 35 (1988) 511–516.

[5] S. V. Kershaw, S. Gilmour, S. Cassidy, P. Pantelis, R.A. Pethrick, J.N. Sherwood, J. Mater. Chem. 2 (1992) 979–981.

[6] R.T. Bailey, F.R. Cruickshank, S. Lochran, D. Pugh, J.N. Sherwood, P.J. Langley, et al. Bull. Mater. Sci. 22 (1999) 421–430.

[7] R.T. Bailey, G.H. Bourhill, F.R. Cruickshank, D. Pugh, J.N. Sherwood, G.S. Simpson, et al. J. Appl. Phys. 75 (1994) 489–492.

[8] R.T. Bailey, F.R. Cruickshank, T.J. Dines, N. Sherwood, M.C. Tedford, J. Raman Spectrosc. 42 (2011) 1174–1184.

[9] R.J. Twieg, C.W. Dirk, IBM Research Report RJ5237 (54077), 1986.

[10] R. Twieg, A. Azema, K. Jain, Y.Y. Cheng, Chem. Phys. Lett. 92 (1982) 208–211.

[11] A.A.A. Kaminskii, Laser crystals and ceramics: recent advances, Laser Photonics Rev. 1 (2007) 93–177.

[12] J.J. Carey, R.T. Bailey, D. Pugh, J.N. Sherwood, F.R. Cruickshank, Appl. Phys. Lett. 81 (2002) 4335-4337.

[13] R.T. Bailey, F.R. Cruickshank, D. Pugh, J.N. Sherwood, J. Phys. D. Appl. Phys. 26 (1993) B208–B216.

[14] P. Kerkoc, R.T. Bailey, F.R. Cruickshank, D. Pugh, J.N. Sherwood, J. Opt. Soc. Am. B. 13 (1996) 2759-2761.

[15] P.J. Langley, R.T. Bailey, F.R. Cruickshank, A.R. Kennedy, S. Lochran, D. Pugh, et al., J. Mater. Chem. 11 (2001) 1047–1056.

[16] P.J. Halfpenny, R.I. Ristić, E.E.A. Shepherd, J.N. Sherwood, J. Cryst. Growth. 128 (1993) 970–975.

[17] P.J. Halfpenny, H. Morrison, R.I. Ristic, E.E.A. Shepherd, J.N. Sherwood, G.S. Simpson, et al., Proc. R. Soc. A Math. Phys. Eng. Sci. 440 (1993) 683–699.

[18] T. Kondo, N. Ogasawara, R. Ito, K. Ishida, T. Tanase, T. Murata, M. Hidai, Sect. C Cryst. Struct. Commun. 44(1988) 102–104.

[19] Cole J M, Goeta A E, Howard J A K, et al. Struct Sci, 58 (2002) 690-700.

[20] R.T. Bailey, F.R. Cruickshank, S. Lochran, D. Pugh, J.N. Sherwood, P.J. Langley, J. D. Wallis, Bull. Mater. Sci. 22 (1999) 421–430.

[21] R.T. Bailey, F.R. Cruickshank, T.J. Dines, N. Sherwood, M.C. Tedford, J. Raman Spectrosc. 42 (2011) 1174–1184.

[22] G.S. Pinheiro, M.N.G. Ferreira Júnior, A.O. dos Santos, P.T.C. Freire, J.A. Lima Jr. C.E.S. Nogueira, L.P. Cardoso, J.N. Sherwood, C.M.R. Remédios, Spectrochim. Acta Part A: Mol. Biomol. Spectrosc. 183 (2017) 209–217.

[23] S. Grimme, J. Comput. Chem. 27 (2006) 1787-1799.

[24] J.P. Perdew, K. Burke, M. Ernzerhof, Phys. Rev. Lett. 77 (1996) 3865.

[25] M.D. Segall, P.L.D. Lindan, M.J. Probert, C.J. Pickard, P.J. Hasnip, S.J. Clark, M.C. Payne, J. Phys. Condens. Matter 14 (2002) 2717.

[26] Junior, M. F., Paraguassu, W., Dos Santos, A. O., & Remédios, C. M. R. Spectrochimica Acta Part A: Mol. Biomo. Spectrosc, 272 (2002) 120944.

[27] Liu Q J, Ran Z, Liu F S, et al., J. Alloy Compd. 631 (2015) 192-201.

[28] M. Born, K. Huang, Dynamical Theory and Experiment I, Springer, Berlin, 1982.

[29] G.V. Sin'ko, N.A. Smirnov, J. Phys.: Condens. Matter 14 (2002) 6989.

[30] G.V. Sin'ko, N.A. Smirnov, J. Phys.: Condens. Matter 16 (2004) 8101.

[31] J. J. Mckinnon, M. A. Spackman, and A. S. Mitchell, Acta Crystallogr., Sect. B: Struct. Sci., Cryst. Eng. Mater. 60 (2004) 627.

[32] P. R. Spackman, M. J. Turner, J. J. Mckinnon, S. K. Wolff, D. J. Grimwood, D. Jayatilaka, and M. A. Spackman, J. Appl. Crystallogr. 54 (2021) 1006-1011.

[33] J. J. McKinnon, D. Jayatilaka, and M. A. Spackman, Chem. Commun. 37 (2007) 3814-3817.

[34] M. A. Spackman and D. Jayatilaka, CrystEngComm. 11 (2009) 19-32.